A&A 628, A88 (2019)
https://doi.org/10.1051/0004-6361/201935966

Astronomy & Astrophysics

GG Tauri A: dark shadows on the ringworld

R. Brauer[1,2], E. Pantin[1], E. Di Folco[3,4], E. Habart[2], A. Dutrey[3,4], and S. Guilloteau[3,4]

[1] CEA Saclay – Service d'Astrophysique, Orme des Merisiers, Bât 709, 91191 Gif-sur-Yvette, France
e-mail: robert.brauer@cea.fr; eric.pantin@cea.fr
[2] Institut d'astrophysique spatiale, CNRS UMR 8617, Université Paris-Sud 11, Bât 121, 91405 Orsay, France
e-mail: emilie.habart@ias.u-psud.fr
[3] Université Bordeaux, Laboratoire d'Astrophysique de Bordeaux, UMR 5804, 33270 Floirac, France
[4] CNRS, LAB, UMR 5804, 33270 Floirac, France

Received 27 May 2019 / Accepted 26 June 2019

ABSTRACT

Context. With its high complexity, large size, and close distance, the ringworld around GG Tau A is an appealing case to study the formation and evolution of protoplanetary disks around multiple star systems. However, investigations with radiative transfer models usually neglect the influence of the circumstellar dust around the individual stars.
Aims. We investigate how circumstellar disks around the stars of GG Tau A influence the emission that is scattered at the circumbinary disk and if constraints on these circumstellar disks can be derived.
Methods. We performed radiative transfer simulations with the POLArized RadIation Simulator (POLARIS) to obtain spectral energy distributions and emission maps in the H-Band (near-infrared). Subsequently, we compared them with observations to achieve our aims.
Results. We studied the ratio of polarized intensity at different locations in the circumbinary disk. We conclude that the observed scattered-light near-infrared emission is best reproduced if the circumbinary disk lies in the shadow of at least two coplanar circumstellar disks surrounding the central stars. This implies that the inner wall of the circumbinary disk is strongly obscured around the midplane, while the observed emission is actually dominated by the upper-most disk layers. In addition, the inclined dark lane ("gap") on the western side of the circumbinary disk, which has been a stable, nonrotating, feature for approximately 20 yr, can only be explained by the self-shadowing of a misaligned circumstellar disk surrounding one of the two components of the secondary close-binary star GG Tau Ab.

Key words. polarization – radiative transfer – protoplanetary disks – binaries: close – circumstellar matter – stars: individual: GG Tauri A

1. Introduction

The formation of stars and their surrounding disks due to a collapse of a molecular cloud is still an ongoing topic of research (e.g., Petr-Gotzens et al. 2015; Dutrey et al. 2016). For instance, a significant number of stars seem to be formed as multiple star systems with one or more additional stars (e.g., Duquennoy & Mayor 1991; Kraus & Hillenbrand 2009; Wurster et al. 2017). Compared to disks around a single star, these systems are able to host a common circumbinary disk as well as disks around their individual stars, which depends strongly on the separation of their stellar components (e.g., Dutrey et al. 2016). Due to the various physical conditions and increased dynamical complexity of these multiple star systems, additional scientific questions have to be addressed. The main questions to be posed are how planets can be formed in either the circumbinary or the circumstellar disks and how these disks and their stars are interacting with each other via radiation and gravitation.

One of the best subjects with which to investigate these questions is the multiple star system, GG Tau A, owing to its close distance and large size (d = 140 pc, see Dutrey et al. 2016 for a recent review of the system characteristics). GG Tau A has a central binary consisting of at least two stars, and a ring-like circumbinary disk with an extent from 190 to 260 au (see Figs. 1 and 2 for illustration; Duchêne et al. 2004; Dutrey et al. 2016). In addition, it is part of a wide binary with GG Tau B (separation ~1400 au, White et al. 1999). Many physical conditions and characteristics of the GG Tau A system were constrained by previous observations at multiple wavelengths (Guilloteau et al. 1999; White et al. 1999; Di Folco et al. 2014; Dutrey et al. 2014a, 2016). However, several important issues are still not fully understood. For example, with the recent finding that the star GG Tau Ab could be a close binary consisting of the stars Ab1 and Ab2, new questions with regard to the possible circumstellar disks around these stars arise (Di Folco et al. 2014). However, the spatial resolution of current instruments and observatories is only sufficient to detect but not resolve them.

In this study, we performed radiative transfer (RT) simulations to derive constraints on the structure and orientation of the circumstellar disks by comparing simulated emission maps and spectral energy distributions with observations. In contrast to previous studies, we considered the circumstellar disks as spatially resolved in our model of GG Tau A. This allowed us to study the impact of the structure and orientation of the circumstellar disks on the surrounding circumbinary disk by casting shadows in the scattered light and by influencing the heating of the circumbinary disk. For example, the binary system HD142527 exhibits shadows due to misaligned inner disks (Casassus et al. 2019). Even some single stars show similar effects (e.g., RXJ1604.3-2130, Pinilla et al. 2018). We performed the radiative transfer simulations with the RT code POLArized RadIation Simulator (POLARIS, Reissl et al. 2016;

Brauer et al. 2017), which was recently updated to consider complex structures of circumstellar disks (Brauer et al., in prep.).

We structured our study as follows. We begin with a description of the radiative transfer code that we used for our simulations in Sect. 2. Subsequently, we introduce the model of GG Tau A, which includes the inner circumstellar disks as well as the surrounding circumbinary disk in Sect. 3. Then, we present our results and investigate the impact of the circumstellar disks on the emission of the circumbinary disk in Sect. 4. Finally, we summarize our conclusions in Sect. 5.

2. The RT code POLARIS

We applied the three-dimensional continuum RT code POLARIS (Reissl et al. 2016; Brauer et al. 2017). It solves the radiative transfer problem self-consistently with the Monte Carlo method. The main applications of POLARIS are the analysis of magnetic fields, by simulating the polarized emission of elongated aligned dust grains, and Zeeman split spectral lines. However, recent developments added circumstellar disk modeling as a new main application of POLARIS (Brauer et al., in prep.).

We used POLARIS to calculate the spatial dust temperature distribution of our GG Tau A model and to calculate emission maps as well as spectral energy distributions based on the thermal emission of the dust grains and the stellar emission scattered at the dust grains. The dust grains that are considered are described in Sect. 3.4. The code was recently published on the POLARIS homepage[1]. For reference, the simulations in this study were performed with the version 4.03. of POLARIS.

3. Model description

Our theoretical model of GG Tau A consists of three stars (Aa, Ab1, and Ab2), each optionally surrounded by a circumstellar (CS) disk, and a large circumbinary (CB) disk that surrounds all stars. We consider the stellar component GG Tau Ab to be a binary (Ab1 and Ab2), based on the findings of Di Folco et al. (2014). In the following, we describe each part of our radiative transfer model with their individual characteristics and parameters that we obtained from various studies.

3.1. Stars

We consider the stars GG Tau Aa, Ab1, and Ab2 as emitting black bodies with an effective temperature and luminosity. The effective temperature of the stars is obtained from their derived spectral type (Kaler 1997). For the stellar luminosities, the photospheric and accretion contributions are combined in a single luminosity (Hartigan & Kenyon 2003; Di Folco et al. 2014). Furthermore, the luminosities of Ab1 and Ab2 are obtained by taking the derived luminosity for Ab from the work of Hartigan & Kenyon (2003) and distributing it to Ab1 and Ab2 via their luminosity ratio ($L_{\rm Ab1}/L_{\rm Ab2} \sim 2$, Di Folco et al. 2014). For comparison purposes with the observations, we took the foreground extinction at all simulated wavelengths into account by using typical extinction curves for dust grains in the interstellar medium and the derived visual extinction $A_{\rm V} = 0.3$ (Weingartner & Draine 2001; Duchêne et al. 2004). Even though a higher visual extinction was derived for Ab1 and Ab2, we assume that this increase is due to local dust in the line-of-sight. The configuration of Ab1 and Ab2 in the simulations (see Fig. 2) corresponds to the reported orientation at the time of their discovery in the winter of 2012. The parameters of the stars are summarized in Table 1.

Table 1. Parameters of stars GG Tau Aa, Ab1, and Ab2.

Stellar parameter		Value	Ref.
GG Tau Aa			
Spectral type		M0	2
Effective temperature	$T_{\rm Aa}$	3700 K	6
Stellar luminosity	$L_{\rm Aa}$	0.38 $L_\odot$	3
Stellar accretion luminosity	$L^{\rm acc}_{\rm Aa}$	0.122 $L_\odot$	3
Visual extinction	A_V	0.3	3
GG Tau Ab1			
Spectral type		M2V	2
Effective temperature	$T_{\rm Ab1}$	3300 K	6
Stellar luminosity	$L_{\rm Ab1}$	0.133 $L_\odot$	2,3
Stellar accretion luminosity	$L^{\rm acc}_{\rm Ab1}$	0.053 $L_\odot$	2,3
Visual extinction	A_V	0.45	3
GG Tau Ab2			
Spectral type		M3V	2
Effective temperature	$T_{\rm Ab2}$	3100 K	6
Stellar luminosity	$L_{\rm Ab2}$	0.067 $L_\odot$	2,3
Stellar accretion luminosity	$L^{\rm acc}_{\rm Ab2}$	0.026 $L_\odot$	2,3
Visual extinction	A_V	0.45	4
Position/Distance			
Distance to GG Tau A	d	140 pc	2,5
Inclination	i	37°	4
Separation* (Aa → Ab)	$r_{\rm Aab}$	43 au	2
Separation* (Ab1 → Ab2)	$r_{\rm Ab12}$	5 au	2
Position angle*	$\rm PA_{stars}$	335°	1

Notes. The parameters with (*) are de-projected to obtain the correct values for the model space (see Fig. 1). The definitions of the position angle and inclination are illustrated in Fig. 2.

References. (1) Yang et al. (2017); (2) Di Folco et al. (2014); (3) Hartigan & Kenyon (2003); (4) Duchêne et al. (2004); (5) White et al. (1999); (6) Kaler (1997).

3.2. Circumstellar disks

Interferometric observations in the infrared and at millimeter wavelengths detected a disk around the GG Tau Aa star with an outer radius of $R_{\rm out} \sim 7$ au (Guilloteau et al. 1999; Dutrey et al. 2014a). Furthermore, in the work of Di Folco et al. (2014), they derived a maximum extent of possible CS disks around the stars Ab1 and Ab2 ($R_{\rm out} \lesssim 2$ au). It is expected that these disks have similar density and temperature distributions as the inner part of circumstellar disks around T Tauri stars (Dutrey et al. 2016). CS disks around the stars are also in agreement with the observations of Yang et al. (2017), which clearly show that dust is present around these stars (see Fig. 5). Previous studies that performed RT simulations usually neglected the influence of the CS disks around the stars. The work of Wood et al. (1999) partially included the influence of the CS disks in their simulations, but they were only able to use a simple approximation due to the limited computational resources at that time. In this study, we included the CS disks around the stars in our radiative transfer model and investigated their influence on the emission of GG Tau A. To successfully decipher the influence of each individual CS disk, we used different models of GG Tau A, which cover all

[1] http://www1.astrophysik.uni-kiel.de/~polaris/

Table 2. Various configurations of our GG Tau A model to investigate influence of each individual circumstellar disk around stars Aa, Ab1, and Ab2 on the emission of circumbinary disk.

#	Configuration	CS disks around:	Aa	Ab1	Ab2
1	No circumstellar disks		–	–	–
2	Disk around Aa		✓	–	–
3	Disk around Ab1		–	✓	–
4	Disk around Ab2		–	–	✓
5	Disks around Aa and Ab1		✓	✓	–
6	Disks around Aa and Ab2		✓	–	✓
7	Disks around Ab1 and Ab2		–	✓	✓
8	Disks around all stars		✓	✓	✓
9	Vertical disk around Ab2		✓	✓	$✓^i$

Notes. Each star is either surrounded by its circumstellar disk (✓) or has no surrounding dust (–). The CS disk with $✓^i$ has an inclination of $i = 90°$ with respect to the plane of the CB disk and a position angle of the rotation axis of 270°.

combinations of disks around the stars Aa, Ab1, and Ab2 (see Table 2).

In the absence of measurements, we considered a density distribution for the CS disks with a radial decrease based on the work of Hayashi (1981) for the minimum mass solar nebular. Combined with a vertical distribution due to hydrostatic equilibrium similar to the work of Shakura & Sunyaev (1973), we obtained the following equation:

$$\rho_{\rm disk} = \rho_0 \left(\frac{r}{R_{\rm ref}}\right)^{-a} \exp\left(-\frac{1}{2}\left[\frac{z}{H(r)}\right]^2\right). \quad (1)$$

Here, r is the radial distance from the central star in the disk midplane, z is the distance from the midplane of the disk, $R_{\rm ref}$ is a reference radius, and $H(r)$ is the scale height. The density ρ_0 is derived from the disk dust mass. The scale height is a function of r as follows:

$$H(r) = h_0 \left(\frac{r}{R_{\rm ref}}\right)^{b}. \quad (2)$$

The exponents a and b set the radial density profile and the disk flaring, respectively (with $a = 3\,[b - 0.5]$ based on Shakura & Sunyaev 1973). The extent of the disk is constrained by the inner radius $R_{\rm in}$ and the outer radius $R_{\rm out}$. An overview of the considered parameters of the CS disks can be found in Table 3. These parameters are chosen to be in agreement with previous studies of GG Tau A. Even though parameters like disk flaring and scale height were not previously derived, they strongly influence the disk emission at $\lambda \in [5\,\mu{\rm m}, 50\,\mu{\rm m}]$. Therefore, we estimated these disk parameters by using individual disk models and comparing their emission at $\lambda = 10\,\mu$m to observations.

3.3. Circumbinary disk

Observations of the CB disk around the stars of GG Tau A show an almost smooth and continuous ring-like dust distribution with brightness variations that are usually caused by the subtraction of the point spread function (PSF), the scattering phase function of the dust grains, and the inclination of the disk (e.g., Fig. 5 top left; Duchêne et al. 2004; Yang et al. 2017). Therefore, we approximated the CB disk with an azimuthally symmetric disk density distribution as shown in Eq. (1). The parameters of the density distribution are mainly based on the findings of Duchêne et al. (2004), who included an exponential decrease for the inner edge between 180 and 190 au, as follows:

$$\rho_{\rm disk+edge} = \begin{cases} \rho_{\rm disk}, & 190\,{\rm au} \le r < 260\,{\rm au}, \\ \rho_{\rm disk} \cdot {\rm e}^{\frac{(r-190\,{\rm au})^2}{2R_c^2}}, & 180\,{\rm au} \le r < 190\,{\rm au}. \end{cases} \quad (3)$$

The parameters that we considered for the CB disk in our model are summarized in Table 4. The density distribution of the GG Tau A model, including the CB disk and the (optional) three CS disks, is shown in Fig. 1. We did not consider dust in regions other than the CS and CB disks because significant dust outside of these disks was not detected with ALMA observations (Dutrey et al. 2016).

The sketch in Fig. 2 illustrates the position angles of the stellar separation and the rotation axis of the CB disk inclination.

Table 3. Parameters of circumstellar disks around GG Tau Aa, Ab1, and Ab2.

Disk parameter		Value	Ref.
GG Tau Aa			
Disk dust mass	$M_{\rm dust}$	$1 \times 10^{-5}\,M_\odot$	1
Inner radius	$R_{\rm in}$	0.07 au	2
Outer radius	$R_{\rm out}$	7 au	1
Scale height	h_0	0.7 au	4
Characteristic radius	$R_{\rm ref}$	7 au	4
Radial density exponent	a	2.1	4
Disk flaring exponent	b	1.2	4
GG Tau Ab1 and Ab2			
Disk dust mass (each)	$M_{\rm dust}$	$1 \times 10^{-7}\,M_\odot$	1
Inner radius	$R_{\rm in}$	0.07 au	2
Outer radius	$R_{\rm out}$	2 au	1,2
Scale height	h_0	0.3 au	4
Characteristic radius	$R_{\rm ref}$	2 au	4
Radial density exponent	a	2.4	4
Disk flaring exponent	b	1.3	4

References. (1) Dutrey et al. (2016); (2) Di Folco et al. (2014); (3) Duchêne et al. (2004); (4) model fitting to flux values of McCabe et al. (2002).

Table 4. Parameters of circumbinary disk around GG Tauri A.

Disk parameter		Value	Ref.
Disk dust mass	$M_{\rm dust}$	$1.3 \times 10^{-3}\,M_\odot$	2,4
Inner radius	$R_{\rm in}$	180 au	4
Outer radius	$R_{\rm out}$	260 au	2,4
Scale height	h_0	21 au	3,4,5
Characteristic radius	$R_{\rm ref}$	180 au	3,4,5
Inner edge cutoff	$R_{\rm c}$	2 au	4
Surface density exp.	a	−1.7	4
Disk flaring	b	1.05	
Position angle	${\rm PA_{CB}}$	277°	1

Notes. The definition of the position angle is illustrated in Fig. 2.
References. (1) Yang et al. (2017); (2) Dutrey et al. (2016); (3) Dutrey et al. (2014a); (4) Duchêne et al. (2004); (5) McCabe et al. (2002).

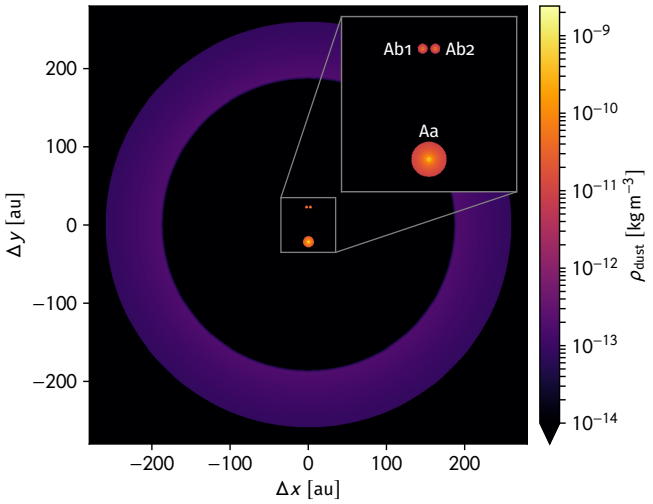

Fig. 1. Dust mass density distribution as cut through midplane of GG Tau A model. The box shows the magnified inner region of the model. The stars Aa, Ab1, and Ab2 are labeled and located in the center of their respective circumstellar disks.

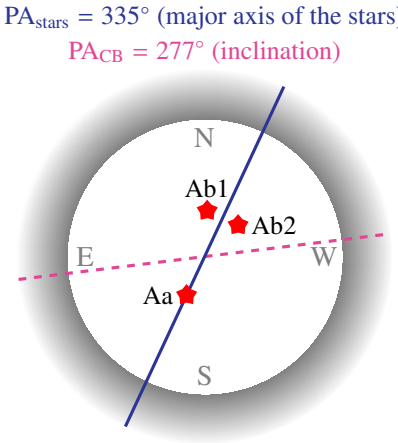

Fig. 2. Sketch of orientations. The separations are not to scale. The blue solid line refers to the position angle of the axis from GG Tau Aa to Ab1 and Ab2. The pink dashed line refers to the major axis of the inclined CB disk. The position angles are celestial positive (N → E). Due to the inclination, the northern region of the disk is oriented toward the observer. The orientation of the Ab1 and Ab2 binary corresponds to its discovery in 2012.

The inner CS disks and the orbit of the stars are in the same plane as the CB disk, unless otherwise noted.

3.4. Dust grains

The material around the GG Tau A stars is composed of gas and dust, whereby the dust grains are mainly responsible for the emission and extinction of radiation. For our simulations, we assumed the dust grains were compact, homogeneous, and spherical and that they consist of 62.5% silicate and 37.5% graphite (MRN-dust, Mathis et al. 1977; optical properties from Weingartner & Draine 2001). Furthermore, we considered the following size distribution of the dust grains (Mathis et al. 1977):

$$\mathrm{d}n(a) \propto a^{p}\mathrm{d}a, \quad a_{\min} < a < a_{\max}. \tag{4}$$

Here, $n(a)$ is the number of dust particles with a specific dust grain radius a. For the CB disk, we assumed that the grain size limits take slightly larger grains ($a_{\max} = 0.5\,\mu$m) into account, which are proposed by the best fit model from the work of Duchêne et al. (2004). However, they obtained these limits from observations in the H-band, which are therefore only valid for dust grains in a certain vertical distance to the midplane. Nevertheless, to avoid additional free parameters, we considered the size limits of these grains for the entire CB disk.

At optical to near-IR wavelengths, the important (not optically thick) line-of-sights from the star to the CB disk pass through the upper layers of the CS disks. Even if grain growth is present in the midplane of the CS disks, the upper layers should still be dominated by small grains. Therefore, we assumed a single grain size limit similar to the ISM for the CS disks. An overview of the considered dust grain parameters is shown in Table 5.

Table 5. Parameters of considered dust grains.

Dust parameter		Value	Ref.
Composition		MRN-dust	1
Minimum size (all disks)	$a_{\min}$	5 nm	1
Maximum size (CS disks)	$a_{\max}^{\mathrm{CS}}$	250 nm	2
Maximum size (CB disk)	$a_{\max}^{\mathrm{CB}}$	500 nm	1
Size exponent	p	−3.5	1

References. (1) Duchêne et al. (2004); (2) Mathis et al. (1977).

3.5. Grid resolution

In our radiative transfer simulations, we fully considered the CS disks in addition to the large outer CB disk. This requires a numerical model, that is a grid that resolves the disk structures on different scales (from ∼0.01 to ∼10 au). We realized this by using a cylindrical grid and adjusting the grid resolution according to the position in the model. With this approach, we were able to resolve the small-scale structures of the circumstellar disks without overly resolving the large-scale structure of the CB disk. In the following, we describe the resolution of our grid along its three cylindrical axis, which is also illustrated in Fig. 3.

The radial cell borders are linearly spaced with 250 cells between 13 and 30 au for the CS disks ($\Delta r \sim 0.07$ au); 50 cells are exponentially distributed between 180 and 260 au for the CB disk ($\Delta r \in [0.7\,\mathrm{au}, 3\,\mathrm{au}]$). In the azimuthal direction, we used two different resolutions. For the CS disks, we used 600 cells in the azimuthal direction ($\Delta a \in [0.13\,\mathrm{au}, 0.3\,\mathrm{au}]$). Also, for the CB disk, we used 180 cells in the azimuthal direction ($\Delta a \in [6\,\mathrm{au}, 9\,\mathrm{au}]$). In the vertical direction, we distributed 251 cells with a vertical extent of 3 au for the CS disks ($\Delta z \sim 0.012$ au). For the CB disk, we distributed the 251 cells in the vertical direction to include ten times the scale height (see Eq. (2) of the disk at each radial distance ($\Delta z \in [0.8\,\mathrm{au}, 1.2\,\mathrm{au}]$).

The center of our cylindrical grid was chosen to be in the middle between the stars Aa and Ab (middle between Ab1 and Ab2). This center point is well suited to provide a similar grid resolution to all CS disks and it is still close to the barycenter of the stars. Nevertheless, other publications may consider different reference points (e.g., centered on Aa), which has to be taken into account when comparing our findings to their work.

4. Comparison with observations

In the following sections, we compare the simulated emission maps and spectral energy distributions of our model with

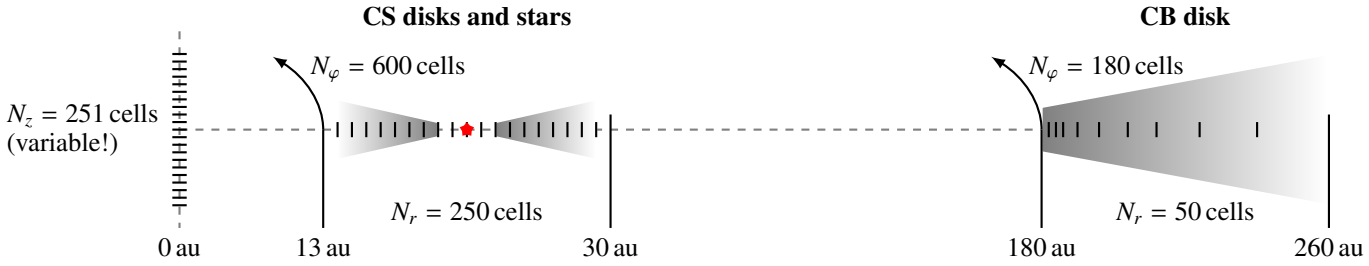

Fig. 3. Distribution of grid cells to resolve circumstellar and circumbinary disks with our numerical model of GG Tau A. The grid is created with cylindrical geometry (radial: r, azimuthal: φ, and vertical: z). The cells in z-direction have a variable vertical size to fit to the local density distribution (see Sect. 3.5). Even if only the circumstellar disk around GG Tau Aa is shown, the same distribution of cells applies to the disks around GG Tau Ab1 and Ab2.

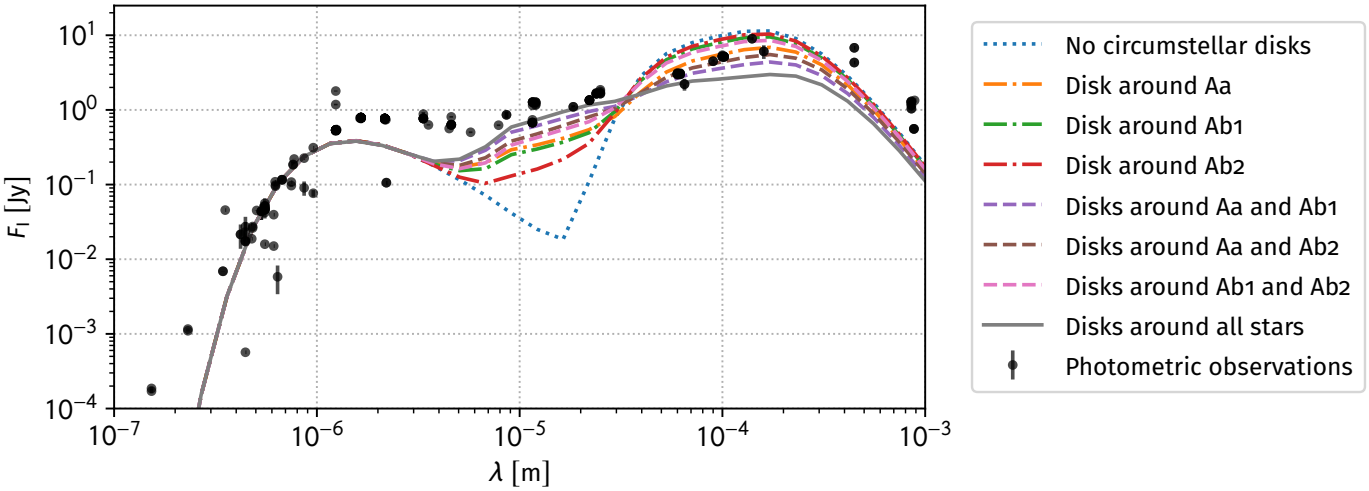

Fig. 4. Spectral energy distribution of GG Tau A disk model. Each energy distribution considers a different combination of the circumstellar disks, but always takes the emission of the circumbinary disk as well as the emission from all three stars into account (see Table 2). For comparison purposes with the observations, the foreground reddening was applied to the simulated spectral energy distributions (A_V = 0.3, Hartigan & Kenyon 2003). The black dots are photometric measurements obtained from the VizieR catalog service (see Appendix A).

observations. Furthermore, we investigate the influence of the CS disks around the stars GG Tau Aa, Ab1, and Ab2 on the emission of the surrounding CB disk.

4.1. Spectral energy distributions

We simulated the spectral energy distribution of our GG Tau A models and compared them with photometric observations that were performed from visual to millimeter wavelengths. In particular, these models consist of the CB disk; the stars Aa, Ab1, and Ab2; and different combinations of the CS disks around these stars (see Table 2).

As illustrated in Fig. 4, the CS disks dominate the emission around $\lambda = 10\,\mu$m and are necessary to obtain a level of emission as measured in observations. The underestimation of the observed photometric flux between $\lambda = 1\,\mu$m and $\lambda = 10\,\mu$m can be related to the usually higher dust temperatures of CS disks in multiple star systems. This is due to accretion shocks from streamers and the stochastically heated emission of probably present nanometer-sized dust grains, as neither of them is taken into account in our simulations (Draine & Li 2001; Dutrey et al. 2016). The underestimation is also related to the well-known missing near-infrared flux problem that motivated the proposition of puffed-up inner rim models. However, this more complicated structure is not taken into account due to the limitations of our grid. Furthermore, the CS disks have also a significant impact on the heating of the CB disk and, therefore, on its (sub-)mm emission. From no CS disk to all CS disks, this emission decreases by a factor of up to five (e.g., $T_{\rm dust}$ = 15 K → 10 K at 250 au). Nevertheless, the slope in the mm range of our simulated spectral energy distributions is steeper than in the observations, which is caused by our assumption of a single grain size distribution of relatively small dust grains in the entire CB disk. This assumption is sufficient for our simulations in the near-IR, but these dust grains underestimate the emission in the mm range. In summary, the impact of the CS disks around the stars in multiple star systems needs to be taken into account when deriving constraints from the infrared to (sub)mm wavelengths range of observed spectral energy distributions.

4.2. Near-infrared emission maps

In this section, we compare simulated polarized emission maps[2] of our GG Tau A model with a polarimetric observation in

[2] In addition to the polarized emission maps, we also simulated intensity maps that we compare to an observation made by Gemini and Hokupa'a (see Figs. B.1 and B.2). For this observation, we unfortunately only have access to the image and not the data, thus our potential for comparison is quite low. Nevertheless, we performed the same analysis on the simulated emission maps and found qualitatively the same behavior as we obtained from the polarized emission maps (see Tables B.1–B.3).

the near-infrared made by Subaru/HiCIAO (see Figs. 5–7, Yang et al. 2017). The simulated emission maps are based on our GG Tau A model in its various configurations as described in Table 2 and Sect. 3. With these configurations, we were able to investigate and identify the impact of each CS disk on the emission of the CB disk. To further quantify our results, we defined six characteristic regions in the emission maps and obtained their mean emitted (polarized) flux by spatially averaging the emission coming from the corresponding circles in Figs. 5–7 (circle radius $r_{\rm circle} = 0.15''$, see Table 6). Regions 2, 3, and 6 are the upper layers of the CB disk, whereas regions 1, 4, and 5 are located on the midplane in the vertical wall of the CB disk. Regions 4, 5, and 6 represent specific locations of projected shadows by individual CS disks. For each region, we calculated the relative decrease of emission from the configuration without any CS disk to any other configuration (see Table 7). In addition, we present selected emission ratios between the characteristic regions for each configuration in Table 8.

4.2.1. Large-scale structures

The absolute polarized intensity in the midplane at the vertical wall of the CB disk (region 1) can be reduced by a factor of 4 to 10 (and up to 300), depending on the number of CS disks in the system (configurations 2, 5, and 8). We lack calibrated PI values to make a direct, absolute comparison with the measured intensities. However, a first robust conclusion is that two disks around Aa and Ab1 (or Ab2) (configurations 5 and 6) are necessary to reproduce the intensity ratios between the midplane and the upper layers (PI_1/PI_2 and PI_1/PI_3). The upper layers of the CB disk are less affected than the midplane: region 2 (most distant layer, rear side of the CB disk) is almost unchanged whatever the configuration, and region 3 (closest to the observer) has intensities reduced by a factor 2 to 4 only. The scale heights of the CS disks have been tuned to maximize the obscuration in the wall of the CB disk without impacting much of the upper-most layers, which still show prominent emission in the observed scattered-light images[3]. It is important to note that our assumption of a vertical wall for the CB disk, under the hypothesis of hydrostatic equilibrium, has a strong impact on the global shape of the CB disk emission. The observed emission is much smoother, while the vertical wall produces a more contrasted, peaked emission at the upper edge of the CB disk wall. The strong constraint on the CS disks scale height and flaring would be relaxed in the case of a rounded wall for the inner edge of the CB disk. Moreover, hydrodynamic simulations of binary systems show that depending on binary parameters, the height of the CB disk at its inner edge can vary (e.g., Sotnikova & Grinin 2007). We conclude that the midplane of the CB disk is mostly obscured by the self-shadowing of Aa and Ab1 (or Ab2) disks, and that most of the emission detected in the southern region emanates from the upper layers of the CB disk only.

4.2.2. Small-scale structures

Individual features are also identified in the observations at smaller spatial scales on the CB disk, which our modeling attempts to reproduce. First, region 4 on the southeastern side displays a kink in the CB disk wall, which looks like a deeper shadow compared to the symmetric western side. It is approximately aligned with the main binary Aa-Ab direction. In our simulation, it corresponds to the shadow casted by the CS disk around Aa, whereby the source of light is the close binary Ab1 and Ab2. Its exact location and azimuthal extent depend on whether the irradiation comes from Ab1, Ab2, or both (configurations 2, 5, and 6). It appears more contrasted than when one of the stars, Ab1 or Ab2, has no disk (or if this third disk is inclined with respect to the CB disk midplane, see item 3 below). In our modeling, this shadow is located exactly on the CB disk midplane since the stellar orbits are coplanar with the CB disk, but small (1–3°) deviations of the orbital inclination could shift it toward upper layers, as seen in the observation. Second, a similar feature can be seen in region 5 (western side, midplane) in our simulations, which corresponds to the shadow casted by the disk of Ab2, illuminated by the star Ab1. There is no clear counterpart in the observations; however, a sharp shadow seems to be projected close to this location on the upper-most layers of the CB disk (region 6).

Finally, the tilted dark lane in region 6 actually looks like a prolongation of an east-west bar, which is aligned with the close binary Ab1 and Ab2, and may extend up to the eastern side of the CB disk (small kink observable at the symmetric location with respect to Ab1 and Ab2). Our modeling can roughly reproduce these patterns if one of the CS disks around Ab2, or Ab1, is significantly tilted with respect to the CB disk midplane (see Fig. 7). In this case (configuration 9), the pattern is the self-shadow of Ab2 by its own disk, projected on the upper layers of the disk; its midplane footprint is not visible due to the CB disk inclination and orientation. This so-called vertical disk configuration corresponds to a maximum tilt of 90°. The location of the sharp western shadow is correctly reproduced in the simulation, but it displays a divergent pattern toward the outer disk. The symmetric eastern shadow is also present, but it is even shallower. In addition, it was necessary to increase the grid resolution and the scale height of the CS disk around Aa to achieve a very sharp western shadow ($h_0 = 0.7\,{\rm au} \rightarrow 0.8\,{\rm au}$).

Attributing the sharp shadow pattern, on the western side of the CB disk, to the self-shadowing by Ab2's own disk is also supported by the absence of rotation of this pattern throughout the years. Indeed, it has appeared at almost the same position angle in all optical and near-infrared images for the past 20 yr (Silber et al. 2000; Krist et al. 2002, 2005; Itoh et al. 2002, 2014; Yang et al. 2017). Itoh et al. (2014) claimed that they detected a counter-clockwise rotation (in the opposite direction to the CB disk rotation) between 2001 and 2011 with an amplitude of about 5°, which has not been since confirmed in the most recent high-contrast images (Yang et al. 2017; Keppler et al., in prep.). In our scenario, the pattern projected onto the CB disk would slightly oscillate as Ab2 rotates around the barycenter of the close binary with a small amplitude in the order of 1.4° (projected separation of about 4.5 au at the distance of 180 au). The orbital period of the close binary star is not precisely constrained yet, but it is evaluated in the 15–20 yr range. If the origin of the dark pattern were a shadow of Ab1 casted by the disk of Ab2 (or vice versa), this shadow would rotate at the same azimuthal speed as the close binary itself. In our proposed scenario, only the precession of the disk rotation axis could generate a systematic counter-rotation of the shadow, which usually takes place on timescales longer than the orbital period. Therefore, self-shadowing by a misaligned disk around one of the components of the close binary star seems to be the most convincing configuration to reproduce the observations. Such misaligned disks in a young binary system have already been reported in the recent years (e.g., HK Tau, and

[3] Using different dust properties for the inner disk would result in a different adjustment of the scale heights to obtain the same effect.

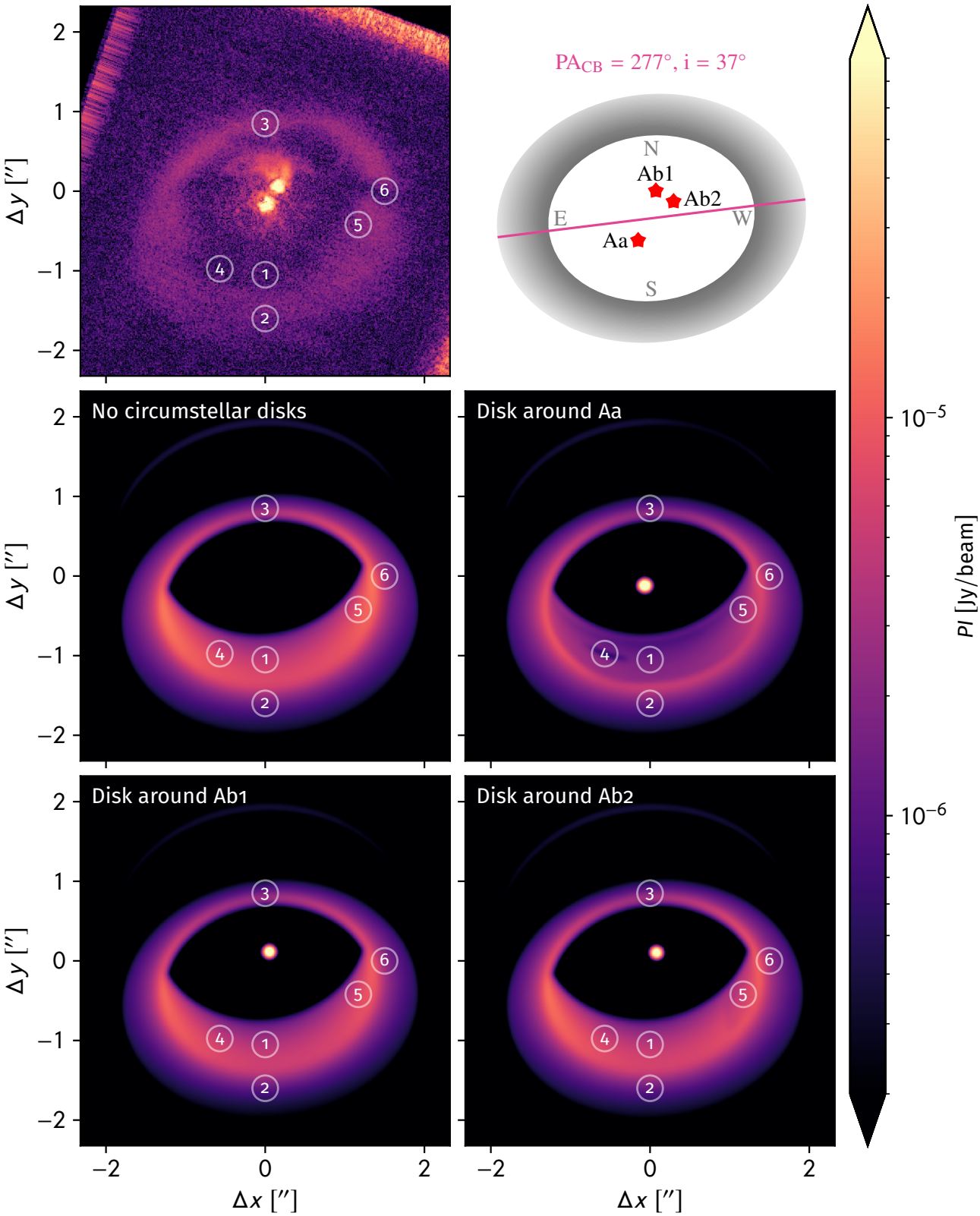

Fig. 5. *Top left*: polarized intensity observation of GG Tau A in near-infrared (*H*-Band) with Subaru/HiCIAO (Yang et al. 2017). The uncalibrated observation was fit visually to the simulated emission maps by assuming a linear photon count. *Other images*: polarized intensity maps of GG Tau A that are simulated at $\lambda = 1.65\,\mu$m. The images are convolved with a Gaussian beam of $0.07'' \times 0.07''$ to take the resolution of the Subaru/HiCIAO telescope into account. Each simulated map considers a different combination of circumstellar disks around GG Tau Aa, Ab1, and Ab2 to investigate their individual influence on the emission of the circumbinary disk (see Table 2). The circles mark regions that are used to derive characteristic flux ratios from the average emission in each circle. Regions 2, 3, and 6 are the upper layers of the CB disk, whereas regions 1, 4, and 5 are located on the midplane in the vertical wall of the circumbinary disk. Regions 4, 5, and 6 represent specific locations of projected shadows by individual CS disks.

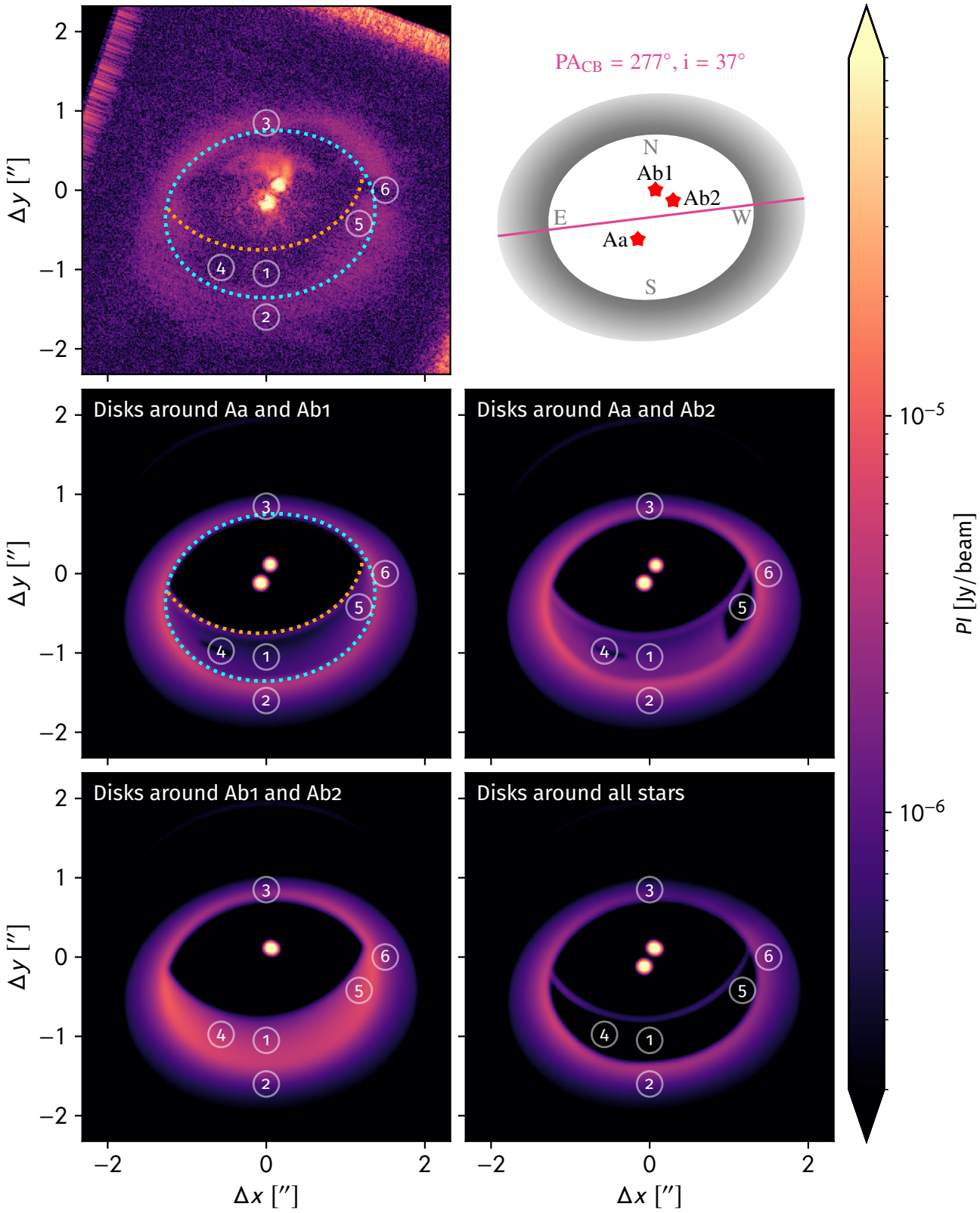

Fig. 6. *Top left*: polarized intensity observation of GG Tau A in near-infrared (*H*-Band) with Subaru/HiCIAO (Yang et al. 2017). The uncalibrated observation was fit visually to the simulated emission maps by assuming a linear photon count. The inner wall of the CB disk is illustrated by ellipses that are fit to the transition from the inner edge to the upper layers of the CB disk as seen in the simulations (see *center left*). *Other images*: polarized intensity maps of GG Tau A that are simulated at $\lambda = 1.65\,\mu$m. The images are convolved with a Gaussian beam of $0.07'' \times 0.07''$ to take the resolution of the Subaru/HiCIAO telescope into account. Each simulated map considers a different combination of circumstellar disks around GG Tau Aa, Ab1, and Ab2 to investigate their individual influence on the emission of the circumbinary disk (see Table 2).

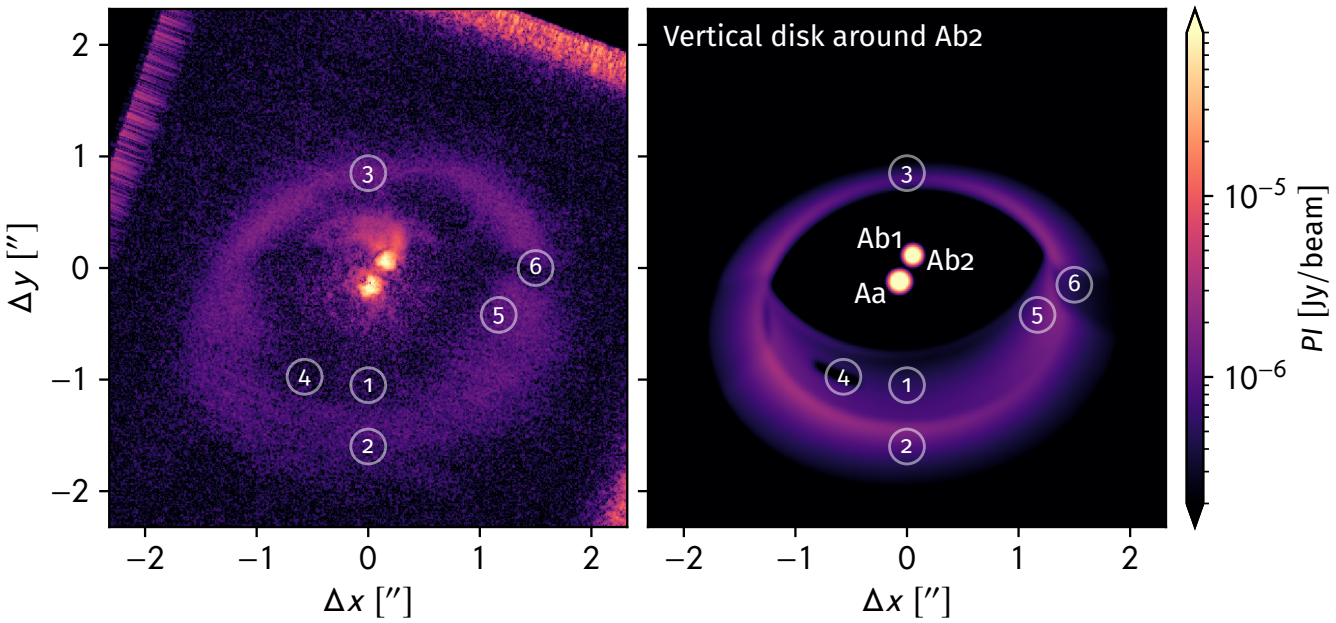

Fig. 7. *Left*: polarized intensity observation of GG Tau A in near-infrared (*H*-Band) with Subaru/HiCIAO (Yang et al. 2017). The uncalibrated observation was fit visually to the simulated emission maps by assuming a linear photon count. *Right*: polarized intensity map of GG Tau A that is simulated at $\lambda = 1.65\,\mu$m. The image is convolved with a Gaussian beam of $0.07'' \times 0.07''$ to take the resolution of the Subaru/HiCIAO telescope into account. The model consists of disks around Aa and Ab1 in the same plane as the circumbinary disk and a disk around Ab2 that is inclined by 90° with a position angle of the rotation axis of 270° (see Fig. 2). An increased grid resolution and sightly larger scale height of the CS disk around Aa was required to achieve the sharp western shadow.

Table 6. Overview of emission at different positions in polarized emission maps (see Figs. 5–7 and Table 2).

#	Configuration	PI_1(Jy)	PI_2(Jy)	PI_3(Jy)	PI_4(Jy)	PI_5(Jy)	PI_6(Jy)
1	No circumstellar disks	4.09×10^{-3}	1.41×10^{-3}	1.64×10^{-3}	5.34×10^{-3}	7.53×10^{-3}	4.06×10^{-3}
2	Disk around Aa	1.28×10^{-3}	1.40×10^{-3}	1.15×10^{-3}	1.20×10^{-3}	2.74×10^{-3}	2.93×10^{-3}
3	Disk around Ab1	3.28×10^{-3}	1.11×10^{-3}	1.30×10^{-3}	4.32×10^{-3}	5.83×10^{-3}	3.04×10^{-3}
4	Disk around Ab2	3.64×10^{-3}	1.25×10^{-3}	1.43×10^{-3}	4.78×10^{-3}	5.08×10^{-3}	3.48×10^{-3}
5	Disks around Aa and Ab1	4.63×10^{-4}	1.09×10^{-3}	8.06×10^{-4}	4.36×10^{-4}	1.03×10^{-3}	1.89×10^{-3}
6	Disks around Aa and Ab2	8.28×10^{-4}	1.23×10^{-3}	9.41×10^{-4}	7.74×10^{-4}	2.62×10^{-4}	2.34×10^{-3}
7	Disks around Ab1 and Ab2	2.84×10^{-3}	9.42×10^{-4}	1.10×10^{-3}	3.76×10^{-3}	4.87×10^{-3}	2.48×10^{-3}
8	Disks around all stars	1.29×10^{-5}	9.29×10^{-4}	5.89×10^{-4}	1.54×10^{-5}	5.43×10^{-5}	1.32×10^{-3}
9	Vertical disk around Ab2	4.65×10^{-4}	8.26×10^{-4}	4.14×10^{-4}	3.70×10^{-4}	9.94×10^{-4}	3.73×10^{-4}

Table 7. Overview of decrease of emission at different positions in polarized emission maps (see Figs. 5–7 and Table 2).

#	Configuration	δPI_1(%)	δPI_2(%)	δPI_3(%)	δPI_4(%)	δPI_5(%)	δPI_6(%)
1	No circumstellar disks	0	0	0	0	0	0
2	Disk around Aa	−69	−1	−30	−78	−64	−28
3	Disk around Ab1	−20	−22	−21	−19	−23	−25
4	Disk around Ab2	−11	−12	−12	−11	−33	−14
5	Disks around Aa and Ab1	−89	−23	−51	−92	−86	−53
6	Disks around Aa and Ab2	−80	−13	−43	−86	−97	−42
7	Disks around Ab1 and Ab2	−31	−33	−33	−30	−35	−39
8	Disks around all stars	−100	−34	−64	−100	−99	−68
9	Vertical disk around Ab2	−89	−41	−75	−93	−87	−91

Notes. The decrease in polarized emission is calculated for each region i and configuration j with $\delta PI_i(j) = \frac{PI_i(j) - PI_i(\text{no disks})}{PI_i(\text{no disks})}$.

Table 8. Overview of ratios between emission at different positions in polarized emission maps (see Figs. 5–7 and Table 2).

#	Configuration	PI_1/PI_2	PI_1/PI_3	PI_1/PI_4	PI_1/PI_5	PI_6/PI_3
1	No circumstellar disks	2.90	2.50	**0.77**	**0.54**	2.48
2	Disk around Aa	**0.91**	1.12	**1.07**	**0.47**	2.55
3	Disk around Ab1	2.96	2.52	**0.76**	**0.56**	2.33
4	Disk around Ab2	2.92	2.54	**0.76**	**0.72**	2.43
5	Disks around Aa and Ab1	**0.42**	**0.57**	**1.06**	**0.45**	2.35
6	Disks around Aa and Ab2	**0.67**	**0.88**	**1.07**	3.15	2.49
7	Disks around Ab1 and Ab2	3.01	2.58	**0.75**	**0.58**	2.26
8	Disks around all stars	0.01	0.02	**0.84**	**0.24**	2.24
9	Vertical disk around Ab2	**0.56**	1.12	**1.26**	**0.47**	**0.90**
10	Observation (Subaru/HiCIAO)	0.73 ± 0.32	0.43 ± 0.16	1.20 ± 0.65	0.48 ± 0.19	0.57 ± 0.17

#	Configuration	PI_1/σ_{BG}	PI_2/σ_{BG}	PI_3/σ_{BG}	PI_4/σ_{BG}	PI_5/σ_{BG}	PI_6/σ_{BG}
10	Observation (Subaru/HiCIAO)	2.9	3.9	6.6	2.4	5.9	3.7

Notes. We obtained the uncertainty of the emission ratios by calculating the standard deviation of the background noise in the observation. In addition, the ratio between the emission of each region and the background noise is shown for the observation at the bottom of the table (background noise: $PI_{BG}/\sigma_{BG} \sim 2$). Each emission ratio that is inside of two sigma of the observed ratio is marked in green (bold) and each other ratio is marked in red (normal).

L1551 NE; Jensen & Akeson 2014; Takakuwa et al. 2017). The entire (∼2″ long) east-west dark bar could be attributed to the self-shadowing by the disk of Ab2 projected onto the accretion streams present in the cavity, which feed the inner CS disks with fresh material from the outer CB disk.

4.3. Implications

Previous studies usually neglected the impact of the CS disks around the stars of GG Tau A (e.g., Duchêne et al. 2004). As a result, the southern region of the CB disk is usually related to the southern inner edge of the CB disk in simulations. A sign of this are the inaccurate distances to the northern and southern regions of the CB disk in the simulation compared to the observation (as seen in Figs. 4 and 5 of Duchêne et al. 2004). As a result, derived quantities such as the scale height and the dust properties can differ greatly from the real values. For instance, the scale height of the CB disk of $h_0 = 21$ au that we used in our model is in good agreement with the observations of Yang et al. (2017) and is much lower than the $h'_0 = 32$ au as used by Duchêne et al. (2004).

Furthermore, the shadow casting by the inner CS disks has an important impact on the temperature structure of the CB disk. From extreme cases of configurations, 1 to 8 in our simulations, the computed temperatures in the disk midplane can be divided by a factor of up to two at the inner edge of the CB disk (from $T_{dust} = 38$ K to $T_{dust} = 17$ K at $R = 180$ au). At a larger distance ($R = 250$ au), the reduction is more moderate (∼30%). This occurs since the heating is dominated by the stellar irradiation impinging the upper disk layers, which are less affected by the shadowing effect. We note that the calculated midplane dust temperatures of configurations 8 and 9 with strong shadowing are more consistent with the direct determination of the temperature of the mm-sized grains reported by Dutrey et al. (2014b) from ALMA and NOEMA data ($T_{dust} = 14$ K at $R = 200$ au and $T_{dust} = 11$ K at $R = 250$ au).

5. Conclusions

We investigated the multiple star system GG Tau A by using a radiative transfer model that considers not only the CB disk but also the CS disks around the individual stars. By studying the ratio of polarized intensity at different locations in the CB disk, we conclude that the observed scattered-light near-infrared emission is best reproduced when the CB disk lies in the shadow of at least two coplanar CS disks surrounding the central stars. This implies that the inner wall of the CB disk is strongly obscured around the midplane, while the observed emission is actually dominated by the upper-most disk layers. In addition, the inclined dark lane ("gap") on the western side of the CB disk, which has been a stable, nonrotating, feature for approximately 20 yr, can only be explained by the self-shadowing of a misaligned CS disk surrounding one of the two components of the secondary close binary star GG Tau Ab.

From our findings, we conclude that the CS disks around the stars are crucial in understanding the emission of multiple star systems in general. This includes the emission at infrared wavelengths coming from the CS disks itself in addition to the decreased scattered-light emission and heating of the CB disk due to the casting of shadows. For instance, the dust temperature derived from mm observations is more consistent with the structure predicted by configurations using at least two coplanar disks. Furthermore, it is important to know the exact configuration to derive constraints on a multiple star system even on large scales. Otherwise, the origin of emission features can be misleading and, therefore, result in wrong conclusions. For instance, the very high scale height that was derived in previous studies for GG Tau A can be explained by interpreting the southern emission as the inner edge of the CB disk instead of its upper layers.

In summary, multiple star systems like GG Tau A offer complex and diverse environments to study, for instance, the formation of planets. Based on our work, future studies of GG Tau A and multiple star systems in general will be able to more accurately analyze observations and radiative transfer simulations by understanding the importance of the CS disks and their influence on the emission of the whole system.

Acknowledgements. This work was supported by the Labex P2IO project A-JWST-01-02-01+LABEXP2IOPDO and the Programme National de Physique Stellaire (PNPS) of CNRS/INSU co-funded by CEA and CNES. This research

has made use of the VizieR catalogue access tool, CDS, Strasbourg, France. The original description of the VizieR service was published in Ochsenbein et al. (2000).

References

Abrahamyan, H. V., Mickaelian, A. M., & Knyazyan, A. V. 2015, Astron. Comput., 10, 99
Altmann, M., Roeser, S., Demleitner, M., Bastian, U., & Schilbach, E. 2017, A&A, 600, L4
Ammons, S. M., Robinson, S. E., Strader, J., et al. 2006, ApJ, 638, 1004
Andrews, S. M., Rosenfeld, K. A., Kraus, A. L., & Wilner, D. J. 2013, ApJ, 771, 129
Andruk, V. M., Pakuliak, L. K., Golovnia, V. V., et al. 2016, Kinemat. Phys. Celest. Bodies, 32, 260
Bianchi, L., Herald, J., Efremova, B., et al. 2011, Ap&SS, 335, 161
Bianchi, L., Shiao, B., & Thilker, D. 2017, ApJS, 230, 24
Brauer, R., Wolf, S., Reissl, S., & Ober, F. 2017, A&A, 601, A90
Casassus, S., Pérez, S., Osses, A., & Marino, S. 2019, MNRAS, 486, L58
Chambers, K. C., Magnier, E. A., Metcalfe, N., et al. 2016, ArXiv e-prints [arXiv:1612.05560]
Cutri, R. M., & Al, E. 2012, VizieR Online Data Catalog: II/311
Cutri, R. M., & Al, E. 2014, VizieR Online Data Catalog: II/328
de Grijp, M. H. K., Lub, J., & Miley, G. K. 1987, A&AS, 70, 95
de Grijp, M. H. K., Keel, W. C., Miley, G. K., Goudfrooij, P., & Lub, J. 1992, A&AS, 96, 389
Dias, W. S., Monteiro, H., Caetano, T. C., et al. 2014, A&A, 564, A79
Di Folco, E., Dutrey, A., Le Bouquin, J.-B., et al. 2014, A&A, 565, L2
Di Francesco, J., Johnstone, D., Kirk, H., MacKenzie, T., & Ledwosinska, E. 2008, ApJS, 175, 277
Draine, B. T., & Li, A. 2001, ApJ, 551, 807
Droege, T. F., Richmond, M. W., Sallman, M. P., & Creager, R. P. 2006, PASP, 118, 1666
Duchêne, G. 2010, ApJ, 709, L114
Duchêne, G., McCabe, C., Ghez, A. M., & Macintosh, B. A. 2004, ApJ, 606, 969
Ducourant, C., Teixeira, R., Périé, J. P., et al. 2005, A&A, 438, 769
Ducourant, C., Le Campion, J. F., Rapaport, M., et al. 2006, A&A, 448, 1235
Duquennoy, A., & Mayor, M. 1991, A&A, 248, A485
Dutrey, A., Di Folco, E., Guilloteau, S., et al. 2014a, Nature, 514, 600
Dutrey, A., Semenov, D., Chapillon, E., et al. 2014b, Protostars and Planets VI (Tucson, AZ: University of Arizona Press), 317
Dutrey, A., Folco, E. D., Beck, T., & Guilloteau, S. 2016, A&ARv, 24
Esplin, T. L., Luhman, K. L., & Mamajek, E. E. 2014, ApJ, 784, 126
Fedorov, P. N., Akhmetov, V. S., & Bobylev, V. V. 2011, MNRAS, 416, 403
Gaia Collaboration (Prusti, T., et al.) 2016, A&A, 595, A1
Gezari, D. Y., Schmitz, M., Pitts, P. S., & Mead, J. M. 1993, NASA RP (Reference Publication)
Guilloteau, S., Dutrey, A., & Simon, M. 1999, A&A, 348, 570
Harris, R. J., Andrews, S. M., Wilner, D. J., & Kraus, A. L. 2012, ApJ, 751, 115
Hartigan, P., & Kenyon, S. J. 2003, ApJ, 583, 334
Hauck, B., Nitschelm, C., Mermilliod, M., & Mermilliod, J.-C. 1990, A&AS, 85, 989
Hayashi, C. 1981, Prog. Theor. Phys. Suppl., 70, 35
Helou, G., & Walker, D. W. 1988, Infrared Astronomical Satellite (IRAS) Catalogs and Atlases, 7, 1
Henden, A. A., Levine, S., Terrell, D., & Welch, D. L. 2015, AAS Meeting Abstracts, 225, 336.16
Herbig, G. H., & Bell, K. R. 1988, Third Catalog of Emission-line Stars of the Orion Population (Santa Cruz: Lick Observatory)
Huber, D., Bryson, S. T., & Al, E. 2017, VizieR Online Data Catalog: IV/34
Ishihara, D., Onaka, T., Kataza, H., et al. 2010, A&A, 514, A1
Ita, Y., Matsuura, M., Ishihara, D., et al. 2010, A&A, 514, A2
Itoh, Y., Tamura, M., Hayashi, S. S., et al. 2002, PASJ, 54, 963
Itoh, Y., Oasa, Y., Kudo, T., et al. 2014, Res. A&A, 14, 1438
Jensen, E. L. N., & Akeson, R. 2014, Nature, 511, 567
Kaler, J. B. 1997, Stars and their Spectra, An Introduction to the Spectral Sequence (Cambridge: University Press)
Kharchenko, N. V. 2001, Kinematika i Fizika Nebesnykh Tel, 17, 409
Kraus, A. L., & Hillenbrand, L. A. 2009, ApJ, 704, 531
Krist, J. E., Stapelfeldt, K. R., & Watson, A. M. 2002, ApJ, 570, 785
Krist, J. E., Stapelfeldt, K. R., Golimowski, D. A., et al. 2005, AJ, 130, 2778
Lasker, B. M., Lattanzi, M. G., McLean, B. J., et al. 2008, AJ, 136, 735
Lawrence, A., Warren, S. J., Almaini, O., et al. 2007, MNRAS, 379, 1599
Marton, G., Tóth, L. V., Paladini, R., et al. 2016, MNRAS, 458, 3479
Mathis, J. S., Rumpl, W., & Nordsieck, K. H. 1977, ApJ, 217, 425
McCabe, C., Duchêne, G., & Ghez, A. M. 2002, ApJ, 575, 974
Mermilliod, J.-C. 1987, A&AS, 71, 413
Mohanty, S., Greaves, J., Mortlock, D., et al. 2013, ApJ, 773, 168
Nascimbeni, V., Piotto, G., Ortolani, S., et al. 2016, MNRAS, 463, 4210
Ochsenbein, F., Bauer, P., Marcout, J., et al. 2000, A&AS, 143, 23
Page, M. J., Brindle, C., Talavera, A., et al. 2012, MNRAS, 426, 903
Petr-Gotzens, M. G., Alcalá, J. M., Spezzi, L., et al. 2015, The Messenger, 162, 42
Pinilla, P., Benisty, M., de Boer, J., et al. 2018, ApJ, 868, 85
Reissl, S., Wolf, S., & Brauer, R. 2016, A&A, 593, A87
Roeser, S., Demleitner, M., & Schilbach, E. 2010, AJ, 139, 2440
Röser, S., Schilbach, E., Schwan, H., et al. 2008, A&A, 488, 401
Saunders, W., Sutherland, W. J., Maddox, S. J., et al. 2000, MNRAS, 317, 55
Shakura, N. I., & Sunyaev, R. A. 1973, A&A, 24, A337
Silber, J., Gledhill, T., Duchêne, G., & Ménard, F. 2000, ApJ, 536, L89
Sotnikova, N. Y., & Grinin, V. P. 2007, Astron. Lett., 33, 594
Strauss, M. A., Davis, M., Yahil, A., & Huchra, J. P. 1990, ApJ, 361, 49
Takakuwa, S., Saigo, K., Matsumoto, T., et al. 2017, ApJ, 837, 86
Takita, S., Kataza, H., Kitamura, Y., et al. 2010, A&A, 519, A83
Tóth, L. V., Marton, G., Zahorecz, S., et al. 2014, PASJ, 66, 17
Urban, S. E., Corbin, T. E., Wycoff, G. L., et al. 1998, AJ, 115, 1212
Weingartner, J. C., & Draine, B. T. 2001, ApJ, 548, 296
White, R. J., Ghez, A. M., Reid, I. N., & Schultz, G. 1999, ApJ, 520, 811
Wood, K., Crosas, M., & Ghez, A. 1999, ApJ, 516, 335
Wurster, J., Price, D. J., & Bate, M. R. 2017, MNRAS, 466, 1788
Yamamura, I., Makiuti, S., Ikeda, N., et al. 2010, VizieR Online Data Catalog: II/298
Yang, Y., Hashimoto, J., Hayashi, S. S., et al. 2017, AJ, 153, 7
Zacharias, N., Monet, D. G., Levine, S. E., et al. 2004a, AAS Meeting Abstracts, 205, 48.15
Zacharias, N., Urban, S. E., Zacharias, M. I., et al. 2004b, AJ, 127, 3043
Zacharias, N., Finch, C. T., Girard, T. M., et al. 2012, VizieR Online Data Catalog: I/322A
Zacharias, N., Finch, C., & Frouard, J. 2017, VizieR Online Data Catalog: I/340

Appendix A: Spectral energy distribution

The black dots in Fig. 4 are photometric measurements obtained from the VizieR catalog service (used catalogs: de Grijp et al. 1987, 1992; Mermilliod 1987; Helou & Walker 1988; Herbig & Bell 1988; Hauck et al. 1990; Strauss et al. 1990; Gezari et al. 1993; Urban et al. 1998; Saunders et al. 2000; Kharchenko 2001; Zacharias et al. 2004a,b, 2012, 2017; Ducourant et al. 2005, 2006; Ammons et al. 2006; Droege et al. 2006; Lawrence et al. 2007; Di Francesco et al. 2008; Lasker et al. 2008; Röser et al. 2008; Duchêne 2010; Ishihara et al. 2010; Ita et al. 2010; Roeser et al. 2010; Takita et al. 2010; Yamamura et al. 2010; Bianchi et al. 2011, 2017; Fedorov et al. 2011; Cutri & Al 2012, 2014; Harris et al. 2012; Page et al. 2012; Andrews et al. 2013; Mohanty et al. 2013; Dias et al. 2014; Esplin et al. 2014; Tóth et al. 2014; Abrahamyan et al. 2015; Henden et al. 2015; Andruk et al. 2016; Chambers et al. 2016; Gaia Collaboration 2016; Marton et al. 2016; Nascimbeni et al. 2016; Altmann et al. 2017; Huber et al. 2017).

Appendix B: Near-infrared observations

Table B.1. Overview of emission at different positions in intensity emission maps (see Figs. B.1 and B.2 as well as Table 2).

#	Configuration	F_1(Jy)	F_2(Jy)	F_3(Jy)	F_4(Jy)	F_5(Jy)	F_6(Jy)
1	No circumstellar disks	8.93×10^{-3}	1.92×10^{-3}	9.76×10^{-3}	9.57×10^{-3}	1.04×10^{-2}	4.86×10^{-3}
2	Disk around Aa	2.76×10^{-3}	1.91×10^{-3}	6.91×10^{-3}	2.15×10^{-3}	4.02×10^{-3}	3.69×10^{-3}
3	Disk around Ab1	7.16×10^{-3}	1.50×10^{-3}	7.42×10^{-3}	7.73×10^{-3}	7.89×10^{-3}	3.72×10^{-3}
4	Disk around Ab2	7.96×10^{-3}	1.69×10^{-3}	8.37×10^{-3}	8.58×10^{-3}	6.75×10^{-3}	4.25×10^{-3}
5	Disks around Aa and Ab1	9.96×10^{-4}	1.48×10^{-3}	4.57×10^{-3}	7.75×10^{-4}	1.50×10^{-3}	2.54×10^{-3}
6	Disks around Aa and Ab2	1.79×10^{-3}	1.68×10^{-3}	5.52×10^{-3}	1.40×10^{-3}	3.52×10^{-4}	3.07×10^{-3}
7	Disks around Ab1 and Ab2	6.20×10^{-3}	1.27×10^{-3}	6.03×10^{-3}	6.74×10^{-3}	6.47×10^{-3}	3.10×10^{-3}
8	Disks around all stars	3.56×10^{-5}	1.25×10^{-3}	3.17×10^{-3}	3.78×10^{-5}	6.99×10^{-5}	1.92×10^{-3}
9	Vertical disk around Ab2	9.93×10^{-4}	1.14×10^{-3}	2.69×10^{-3}	6.52×10^{-4}	1.47×10^{-3}	8.23×10^{-4}

Table B.2. Overview of decrease of emission at different positions in intensity emission maps (see Figs. B.1 and B.2 as well as Table 2).

#	Configuration	δF_1(%)	δF_2(%)	δF_3(%)	δF_4(%)	δF_5(%)	δF_6(%)
1	No circumstellar disks	0	0	0	0	0	0
2	Disk around Aa	−69	−1	−29	−78	−61	−24
3	Disk around Ab1	−20	−22	−24	−19	−24	−24
4	Disk around Ab2	−11	−12	−14	−10	−35	−13
5	Disks around Aa and Ab1	−89	−23	−53	−92	−86	−48
6	Disks around Aa and Ab2	−80	−13	−43	−85	−97	−37
7	Disks around Ab1 and Ab2	−31	−34	−38	−30	−38	−36
8	Disks around all stars	−100	−35	−68	−100	−99	−61
9	Vertical disk around Ab2	−89	−41	−73	−93	−86	−83

Notes. The decrease in emission is calculated for each region i and configuration j with $\delta F_i(j) = \frac{F_i(j) - F_i(\text{no disks})}{F_i(\text{no disks})}$.

Table B.3. Overview of ratios between emission at different positions in intensity emission maps (see Figs. B.1 and B.2 as well as Table 2).

#	Configuration	F_1/F_2	F_1/F_3	F_1/F_4	F_1/F_5	F_6/F_3
1	No circumstellar disks	4.64	0.92	0.93	0.86	0.50
2	Disk around Aa	1.45	0.40	1.29	0.69	0.53
3	Disk around Ab1	4.79	0.97	0.93	0.91	0.50
4	Disk around Ab2	4.70	0.95	0.93	1.18	0.51
5	Disks around Aa and Ab1	0.67	0.22	1.28	0.66	0.56
6	Disks around Aa and Ab2	1.07	0.32	1.28	5.09	0.56
7	Disks around Ab1 and Ab2	4.89	1.03	0.92	0.96	0.51
8	Disks around all stars	0.03	0.01	0.94	0.51	0.61
9	Vertical disk around Ab2	0.87	0.37	1.52	0.67	0.31

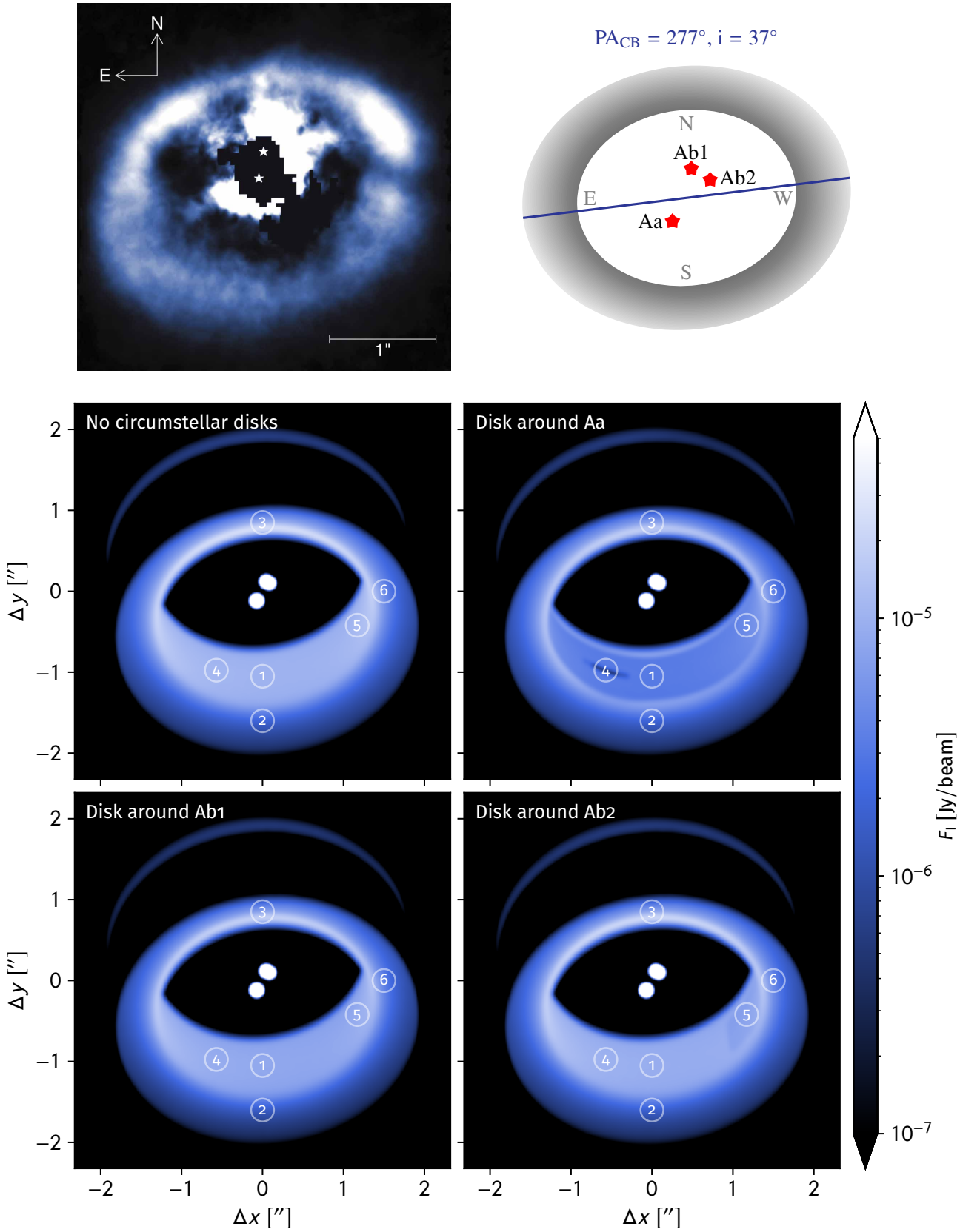

Fig. B.1. *Top left*: observation of GG Tau A in near-infrared (H-Band) with Gemini/Hokupa'a (Credit: Daniel Potter/University of Hawaii Adaptive Optics Group/Gemini Observatory/AURA/NSF). *Other images*: intensity maps of GG Tau A that are simulated at $\lambda = 1.65\,\mu$m. The images are convolved with a Gaussian beam of $0.05'' \times 0.05''$ to take the resolution of the Gemini/Hokupa'a telescope into account. Each simulated map considers a different combination of circumstellar disks around GG Tau Aa, Ab1, and Ab2 to investigate their individual influence on the emission of the circumbinary disk (see Table 2).

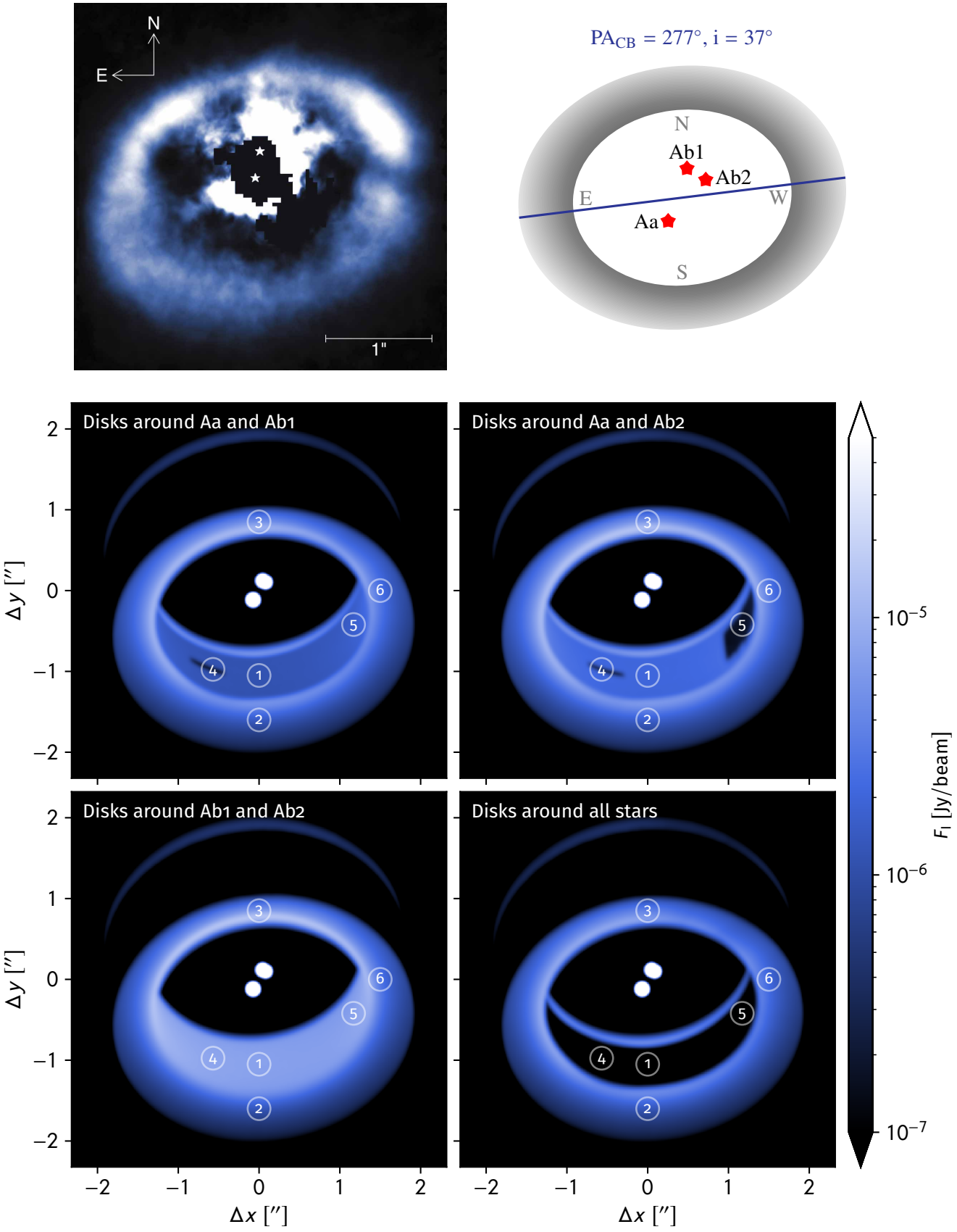

Fig. B.2. *Top left*: observation of GG Tau A in near-infrared (*H*-Band) with Gemini/Hokupa'a (Credit: Daniel Potter/University of Hawaii Adaptive Optics Group/Gemini Observatory/AURA/NSF). *Other images*: intensity maps of GG Tau A that are simulated at $\lambda = 1.65\,\mu$m. The images are convolved with a Gaussian beam of $0.05'' \times 0.05''$ to take the resolution of the Gemini/Hokupa'a telescope into account. Each simulated map considers a different combination of circumstellar disks around GG Tau Aa, Ab1, and Ab2 to investigate their individual influence on the emission of the circumbinary disk (see Table 2).

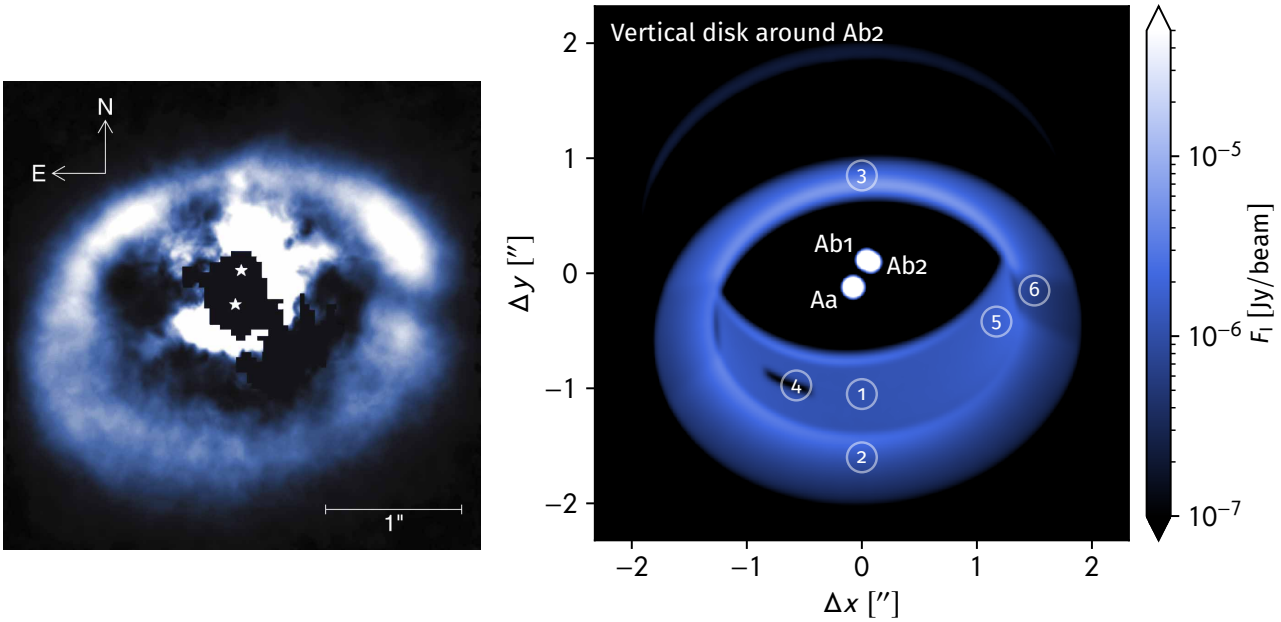

Fig. B.3. *Left*: observation of GG Tau A in near-infrared (*H*-Band) with Gemini/Hokupa'a (Credit: Daniel Potter/University of Hawaii Adaptive Optics Group/Gemini Observatory/AURA/NSF). *Right*: intensity maps of GG Tau A that are simulated at $\lambda = 1.65\,\mu$m. The images are convolved with a Gaussian beam of $0.05'' \times 0.05''$ to take the resolution of the Gemini/Hokupa'a telescope into account. The model consists of disks around Aa and Ab1 in the same plane as the circumbinary disk and a disk around Ab2 that is inclined by 90° with a position angle of the rotation axis of 270° (see Fig. 2).